Available online at www.sciencedirect.com
SCIENCE DIRECT
Polymer 47 (2006) 4182–4193
polymer
www.elsevier.com/locate/polymer

Side chain length dependence on supra-molecular structures in a series of aromatic polyimides having terminal 4-cyanobiphenyl liquid crystalline side chains☆

Jr-Jeng Ruan [a], Shi Jin [b], Jason J. Ge [a], Kwang-Un Jeong [a], Matthew J. Graham [a], Dong Zhang [a], Frank W. Harris [a], Bernard Lotz [c], Stephen Z.D. Cheng [a,*]

[a] *Maurice Morton Institute and Department of Polymer Science, The University of Akron, Akron, OH 44325-3909, USA*
[b] *Department of Chemistry, College of Staten Island, The City University of New York, Staten Island, NY 10314, USA*
[c] *Institut Charles Sadron, 6 Rue Boussingault, Strasbourg 67083, France*

Available online 3 March 2006

Abstract

A series of newly designed polyimides, composed of aromatic polyimide backbones and methylene side chains with terminal 4-cyanobiphenyl groups, were synthesized based on the polycondensation of 3,3′,4,4′-biphenyl tetracarboxylic dianhydride (BPDA) with 2,2′-bis{ω-[4-(4-cyanophenyl)phenyoxy-*n*-alkoxycarbonyl]}-4,4′-biphenyl diamine (*n*CBBP, where *n* is the number of methylene units in the side chains). We report our structural and morphological studies on this series of BPDA–*n*CBBP, which possesses $n=7$, 9, and 11 methylene units in the side chains. For these three polyimides, a nematic (N) phase was first formed at high-temperatures during cooling from the isotropic melt. The transition temperatures and enthalpies were cooling-rate independent as observed in differential scanning calorimetry. This N phase was further confirmed by the results of wide angle X-ray diffraction (WAXD) and polarized light microscopic experiments. At lower temperatures, ordered structures were formed. It was surprising that in the cases of BPDA–*n*CBBP ($n=7$ and 9), triclinic lattices were observed; while in the case of BPDA-11CBBP, a hexagonal lattice was evident, as determined by 2D WAXD experiments. This indicated that by increasing the number of methylene units in the LC side chains, the individual chains (base unit) used in constructing these supra-molecular structures changed their packing symmetry. Namely, when the number of methylene units in the side chains was relatively low (i.e. the length is short), the individual chains were packed into a ribbon-like structure. However, when the side chain length is long enough, the individual chains exhibit cylindrical symmetry. Regardless of the lattice formed by the supra-molecular structures, they are all on the nanometer length scale.

Keywords: 4-Cyanobiphenyl group; Supra-molecular structures; Mesogens

1. Introduction

One of the important and challenging topics in materials chemistry is designing novel supra-molecular structures with dimensions from 1 to 100 nm with synthetic materials via self-assembly/micro-processing technologies for various applications in the biological and electro-optical areas [1]. Ordered self-assembly of block copolymers, dendrimers, liquid crystalline (LC) polymers and polymer brushes exhibits a wide range of new types of supra-molecular nano-structures and morphologies [2–8]. For example, supra-molecular LC structures can be controlled by designing the chemistry of mesogens, which are integrated into different parts of the polymers assembling via chemical and/or physical bonds.

In the past, it seemed difficult for aromatic polyimides to exhibit LC behaviors except for a few examples of main-chain LC poly(ester–imides) or polyimides with aliphatic spacers [9–15]. Recently, we have designed a series of aromatic polyimide backbones having side chains in which methylene units are connected to terminal 4-cyanobiphenyl groups. We expected that these side-chain mesogens may help to stabilize the LC phases. In particular, we are interested in investigating the roles of the aromatic polyimide backbones and LC side chains in forming the stable LC phases, and anticipate that these polymers may provide new insight in constructing supra-molecular structures.

The design of this type of main-chain/side-chain polyimide is based on our recent study of a series of polyesters having side chains containing terminal 4-cyanobiphenyl groups. In the LC side chains, the number of methylene units was between 8 and

☆The occasion of Prof Jim McGrath's 70th birthday for his pioneering contributions and leadership of polymer chemistry.

* Corresponding author. Tel.: +1 330 972 6931; fax: +1 330 972 8626.
E-mail address: scheng@uakron.edu (S.Z.D. Cheng).

0032-3861/$ - see front matter © 2006 Elsevier Ltd. All rights reserved.
doi:10.1016/j.polymer.2006.02.039

11. Structures ranging from low ordered LC phases to three-dimensionally (3D) long-range ordered crystal phases were observed [16–20]. The most important finding was that in this series of main-chain/side-chain LC polyesters, only LC phases can be found in those with an even number of methylene units in the side chains, while supra-molecular 'crystalline' phases exist in those with odd-numbers of methylene units in the side chains. Furthermore, the aromatic polyester backbones and pendent 4-cyanobiphenyls with odd-numbers of methylene units in the side chains cooperatively construct the supra-molecular 'crystal' unit cells. Polymorphism was also found in this series of polyesters, and the most frequently observed supra-molecular 'crystal' unit cells are triclinic with the lowest $P\bar{1}$ symmetry. The driving force to study this series of main-chain/side-chain polyimides is their unique surface alignment characteristics for LC display applications. They can provide tunable high pre-tilt angles at the thin film surfaces [21–25].

In this work, we try to convey the message that self-assembled structures can also be generated in this series of polyimides. We have chosen aromatic polyimides having side chains with three different lengths of methylene units ($n=7$, 9, and 11) and terminal 4-cyanobiphenyl groups. The important issue is to understand the interrelationship and interdependence of the non-LC backbones and the pendent mesogens in the side chains in forming the low-ordered LC phase as well as in constructing the self-assembled supra-molecular crystal structures. Our focus is, in particular, on investigating the ordered phase structures on different length scales using combined experimental techniques and determining the role of side chains in the formation of these ordered structures.

2. Experimental section

2.1. Materials and samples

The key for polymerizing this series of polyimides was to synthesize a new diamine containing pendent 2,2′-bis{ω-[4-(4-cyanophenyl)phenyoxy-*n*-alkoxycarbonyl]}-4,4′-biphenyldiamine (*n*CBBP). Scheme 1 shows this synthetic process in six steps, which was described in Ref. [26]. Polymerization was carried out in one-step via the polycondensation of 3,3′,4,4′-biphenyl tetracarboxylic dianhydride (BPDA) and 2,2′-bis{ω-[4-(4-cyanophenyl)phenyoxy-*n*-alkoxycarbonyl]}-4,4′-biphenyldiamine (*n*CBBP, Scheme 2, $n=7$, 9, and 11). An equal molar ratio of the dianhydride and diamine was put into the reaction. The corresponding polymerization was conducted in

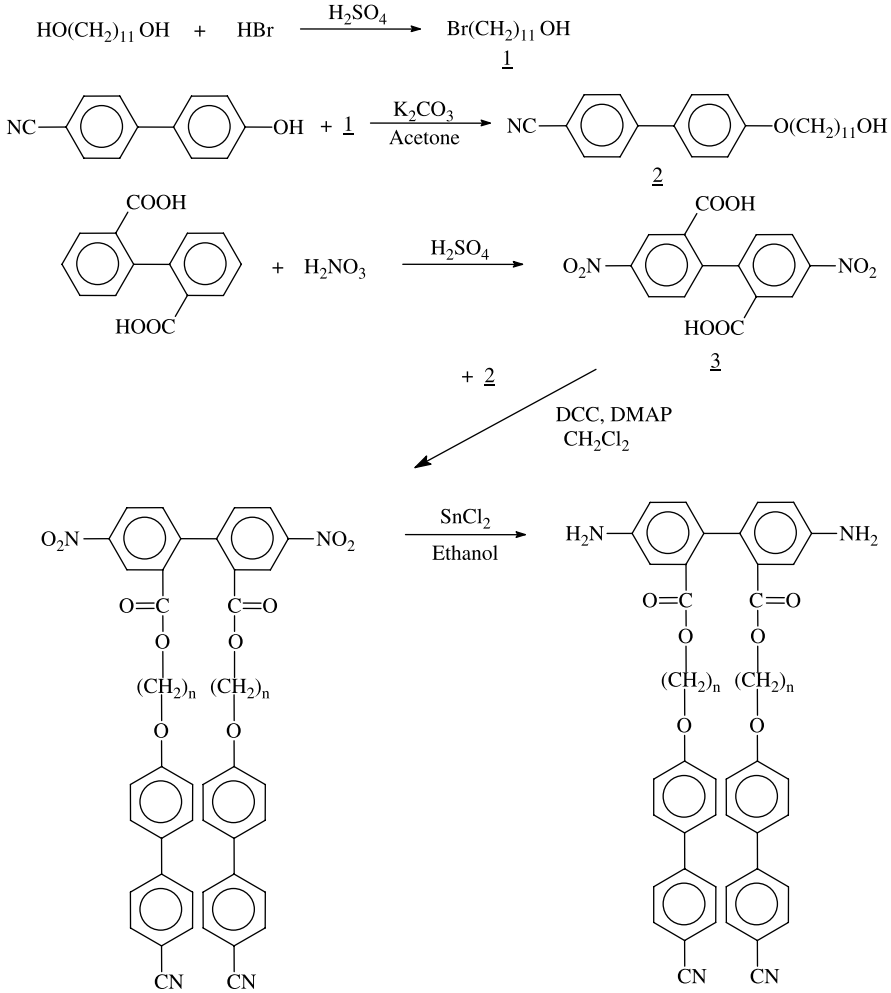

Scheme 1. Synthesis of a diamine containing pendent 2,2′-bis{ω-[4-(4-cyanophenyl)-phenyoxy-11-alkoxycarbonyl]}-4,4′-biphenyldiamine (11CBBP).

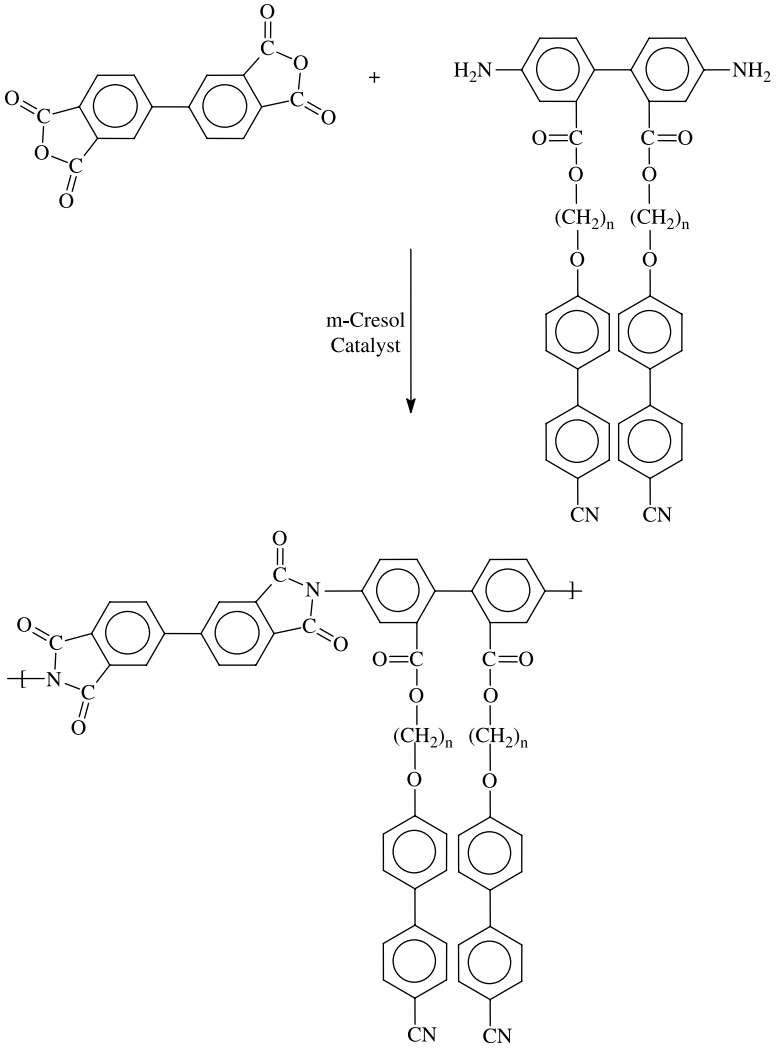

Scheme 2. Synthesis of a polyimide BPDA-11CBBP.

a three-neck flask while refluxing in a solution of *m*-cresol in a dried N_2 atmosphere with a tertiary amine catalyst (isoquinoline) at elevated temperatures (at 185 °C) for 24 h (Scheme 2). The imidiztion process was detected by Fourier transform infrared (FT-IR) and proton nuclear magnetic resonance spectroscopy. For BPDA–*n*CBBP samples, the molecular weight per repeating unit was 1168, 1196, and 1224 g/mol in which 440 g/mol belongs to the aromatic polyimide backbone and 728, 756, and 784 g/mol to the pendent side chains, respectively. The intrinsic viscosities of this series of polymers were 1.05, 1.10, and 1.21 dL/g in *m*-cresol at 50 °C. Their thermal degradation temperatures with a 2% weight loss were at 350–360 °C based on thermogravimetric measurements.

After polymerization, the samples were in powder form. They were melt-pressed into films (length × width × thickness of $15 \times 15 \times 0.1\ mm^3$) and used for differential scanning calorimetry (DSC) and one-dimensional (1D) wide angle X-ray diffraction (WAXD) experiments. The oriented polymer samples were obtained by uniaxially stretching the film samples in their liquid crystalline (LC) state up to about 500% elongation for 2D WAXD experiments. For the polarized Fourier transform infrared (FT-IR) spectroscopy experiments, oriented samples were obtained by mechanically shearing in the LC state. To preparing the polyimide films for polarized light microscopy (PLM), films with thicknesses around 10 μm were made by solution casting concentrated 10% *m*-cresol/NMP (9:1) solutions. The thin film samples for transmission electron microscopy (TEM) experiments were cast from 0.1% *m*-cresol/NMP (9:1) solution onto carbon-coated glass substrates. After drying the sample in vacuum at 170 °C for 1 week, thin films with a thickness of less than 20 nm were obtained. They were annealed at 200 °C for several hours, and then shadowed by Pt. Various annealing conditions were also applied to develop ordered structures in the polymers. Thermogravimetry was used to ensure that the solvent was completely removed in the samples.

2.2. Equipment and experiments

Thermotropic phase transitions were observed in a Perkin–Elmer DSC-7 with a cooling apparatus. The temperature and heat flows were calibrated using standard materials at different

rates between 2.5 and 40 °C/min in dry N_2. When the cooling and heating rates were high, the DSC sample weights were decreased correspondingly to avoid thermal gradients within the samples. A cooling experiment was always carried out first, and a subsequent heating was performed at a rate that was equal to the previous cooling rate. When the phase transitions were characterized, onset temperatures were used as the transition temperatures. For the cooling experiments, the onset temperatures at high-temperature side were used where the beginning of the exothermic process started. During heating, the onset temperatures at low-temperature side were adopted.

Reflection 1D WAXD powder experiments were conducted on a Rigaku 12 kW rotating-anode generator (Cu K_α) coupled with a diffractometer. The diffraction peak positions and widths were calibrated with silicon crystals of known crystal size in the high 2θ-angle region ($>15°$) and silver behenate in the low 2θ-angle region. A hot stage was coupled to the diffractometer in order to study the LC structural evolutions with temperatures at cooling and heating rates of 2.5 °C/min. The temperature of this hot stage was calibrated to be within ± 1 °C. Samples were scanned across a 2θ-angle range of 1.5–35° at a scanning rate of 7°/min. The oriented 2D WAXD patterns were obtained using a Rigaku X-ray imaging system with an 18 kW rotating anode generator. A 30 min exposure time was required for a high-quality pattern. In both 1D and 2D WAXD experiments, background scattering was subtracted.

Phase morphology was examined via a PLM (Olympus BH-2) coupled with a Mettler hot stage (FP-90). In order to confirm existence of the low-ordered LC phase, mechanically sheared film samples were also examined in PLM. A JEOL (1200 EX II) TEM was utilized to study the ordered structures in the nanometer range. An accelerating voltage of 120 kV was used. Selected area electron diffraction (SAED) patterns of the TEM samples having different zones were obtained using a tilting stage to determine the crystal unit-cell symmetry and dimensions. The camera length was set at 50 cm, and the calibration of the ED spacing was performed using the TlCl *d*-spacings and their multiples.

For monitoring chemical bond orientations in the oriented samples, polarized FT-IR experiments of the mechanically sheared films (at 260 °C on a KBr substrate) were conducted on a Mattson Galaxy Series FT-IR 5000 spectrometer equipped with a He:Ne laser source and a polarizer rotation stage in a transmission geometry. The accuracy of the wavenumber is within 4 cm^{-1}. A rotation stage between 0 and 90° was used to control the sample orientation with respect to the polarized IR beam in the azimuthal direction. The calculation of the dichroic ratio ($A_{\parallel}/A_{\perp}$) was carried out using the ratio of the intensity obtained between parallel (0°) and perpendicular (90°) spectra with respect to the orientation direction. The measurements were taken at room temperature.

The sample density measurements were carried out in a density gradient column ranging between 1.2 and 1.4 g/cm^3 at room temperature.

3. Results and discussion

3.1. Phase transitions and their corresponding structural evolutions

Fig. 1(a) and (b) shows two sets of DSC cooling and the subsequent heating diagrams of BPDA–11CBBP at different rates (between 2.5 and 40 °C/min) as an example. Two transition processes can be observed during cooling in

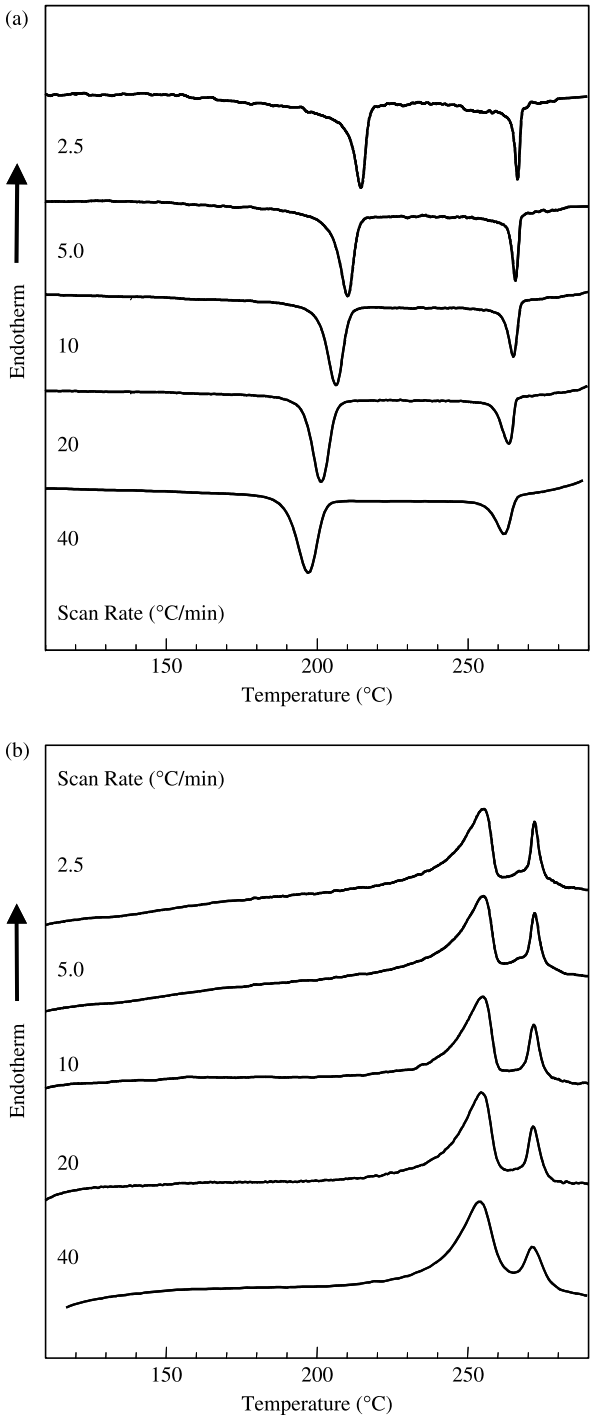

Fig. 1. Two sets of DSC cooling (a) and subsequent heating (b) diagrams for BPDA–11CBBP samples at different rates.

Fig. 1(a). At a cooling rate of 5 °C/min, e.g. the onset temperature of the high-temperature exothermic peak is observed at 268 °C, and the transition enthalpy involved is 2.90 kJ/mol. The onset of the low-temperature exothermic peak is at 217 °C with a transition enthalpy of 6.15 kJ/mol. As the cooling rate increases to 40 °C/min, the onset high-temperature exotherm is almost unchanged while the onset of the low-temperature exotherm decreases to 205 °C. The transition enthalpies of these two processes are cooling rate independent. These observations reveal that the high-temperature phase transition must be associated with a mesophase transition (most likely, a LC phase). On the other hand, the low-temperature exotherm exhibits some degree of cooling-rate dependence, yet its transition enthalpy remains constant at different cooling rates. Such a dependence of the transition temperature but an invariance of the transition enthalpy with respect to the cooling rate may represent a transition associated with supra-molecular structure formation [16,20].

Upon subsequent heating, as shown in Fig. 1(b), both of the transition peak temperatures are at 255 and 272 °C and the transition enthalpies have little dependence on the heating rates. Therefore, the formation of the low-temperature phase requires a substantial undercooling (around 35–50 °C depending upon the cooling and heating rates), while the formation of the high-temperature phase needs only few degrees of undercooling.

Other two BPDA–*n*CBBP ($n=7$ and 9) polyimides exhibit similar transition behaviors. However, with decreasing numbers of methylene units in the side chains, the transition temperatures for the high-temperature phases are pushed higher. In the case of BPDA–7CBBP, the high-temperature transition processes occurs at 330 °C, as shown in Fig. 2 at a heating rate of 20 °C/min. This relatively fast scanning rate was used to avoid sample degradation. However, with a decreasing number of methylene units, the transition temperatures of the low-temperature phases (in both cooling and heating) for this series of BPDA–*n*CBBP polyimides surprisingly decrease. For example, BPDA–7CBBP has a low-temperature phase onset temperature of 190 °C during cooling, while this phase melts during subsequent heating at 225 °C. Therefore, in this series of polyimides, the number of methylene units in the side chain seems to broaden the stability of the high-temperature phases.

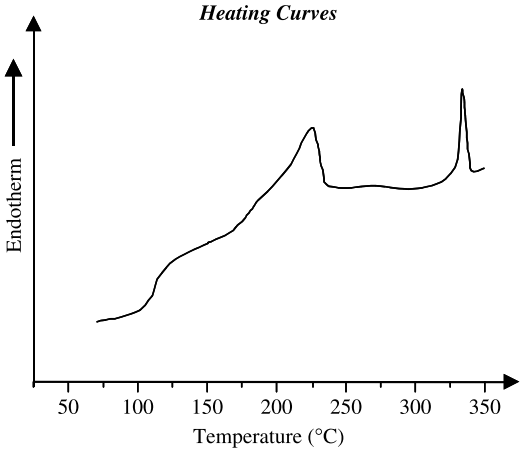

Fig. 2. A DSC heating diagram for BPDA–7CBBP sample at 20 °C/min.

Fig. 3(a) shows a set of WAXD powder patterns for BPDA-11CBBP at different temperatures recorded during cooling at 2.5 °C/min. In this figure, only one wide-angle scattering halo is evident between 300 and 220 °C. This halo indicates that in this temperature region only short-range order exists in molecular lateral packing. At the 267 °C high-temperature transition, no additional diffraction peak appears, yet a sudden change of the *d*-spacing of this halo can be found (as shown in Fig. 3(b)), indicating a first-order transition from the I melt to a low ordered LC phase as reported previously in several LC polymers [8,9,27–30]. Based on the WAXD results in Fig. 3(a), this phase can be identified as an N phase (this is also supported by the PLM results, see below). With decreasing temperatures, the *d*-spacing of the halo scattering slightly but continuously shifts towards smaller 2θ values due to thermal contraction. At

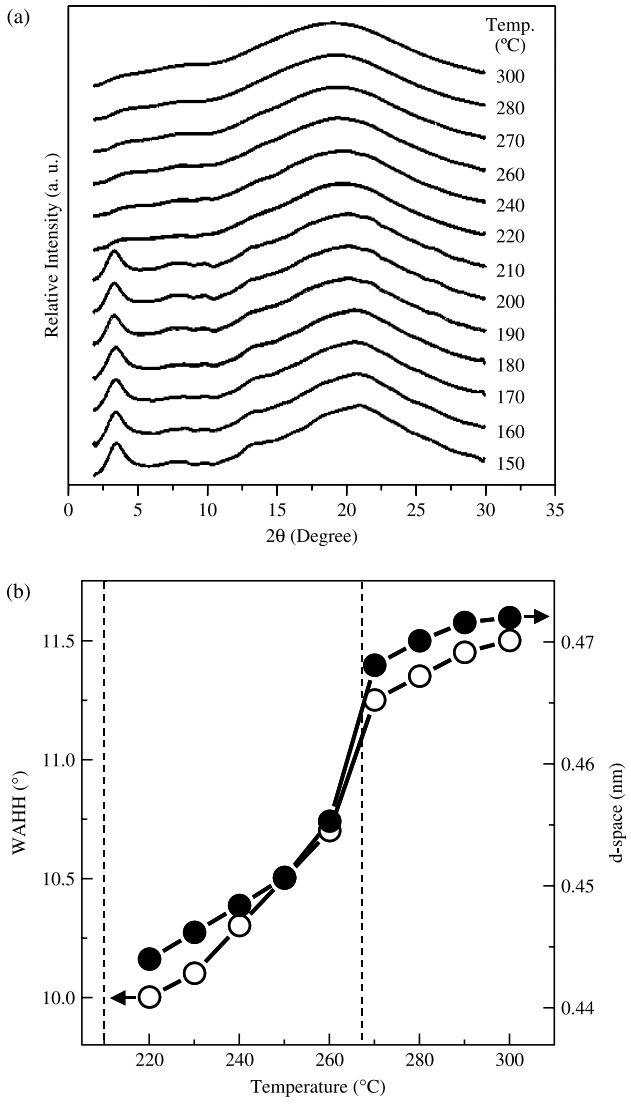

Fig. 3. Set of 1D WAXD powder patterns of BPDA–11CBBP during cooling at different temperatures (cooling rate of 2.5 °C/min) (a); and a plot of a relationship between the *d*-spacing and half-width at half-height of the halo at $2\theta=21°$ and temperature during cooling (b).

210 °C, an intense but relatively broad Bragg reflection at a low-angle of $2\theta = 3.50°$ (d-spacing of 2.54 nm) appears in Fig. 3(a). This indicates that an ordered structure with a length scale of a few nanometers has formed. This diffraction gradually shifts to $2\theta = 3.74°$ (d-spacing of 2.36 nm) when the temperature decreases to 150 °C due to thermal contraction. In the wide-angle region, a scattering halo with a center position at approximately $2\theta = 21.0°$ (d-spacing of 0.423 nm) can be seen. A few weak and diffuse diffractions also appeared when the temperatures were below 210 °C in Fig. 3(a). Among them, the most obvious one is at $2\theta = 13.4°$ (d-spacing of 0.676 nm). The structural origins of these diffractions can be understood only after the investigation of oriented 2D WAXD fiber patterns (Section 3.2). At this moment, we can speculate that the transition at around 210 °C is associated with the formation of an ordered supra-molecular structure during cooling. The 1D WAXD powder pattern upon heating is structurally reversible with those in cooling. However, the low-temperature ordered supra-molecular structure, which is dominantly characterized by the low-angle Bragg reflection, disappears at around 250 °C and enters the N phase.

Fig. 4 shows a set of 1D WAXD powder patterns for BPDA–7CBBP during cooling from 220 °C at 2.5 °C/min. Note that at 220 °C, which is the highest temperature reached in this experiment, BPDA–7CBBP is still in the N LC phase and the I state was not reached (the transition temperature between the N and I phases is at 330 °C, Fig. 2). At 220 °C, except for a scattering halo in the wide-angle region, no Bragg reflections are observed in the entire 2θ angle region studied, indicating that no long-range order exists on any structural length-scale. As the temperature is decreased to below 190 °C, the scattering halo at $2\theta = 21°$ (d-spacing of 0.423 nm) in the wide-angle region exhibits a small but sudden change. At the same time, a low-angle diffraction peak starts to appear. Both of these two observations correspond to the exothermic low-temperature transition peak observed in DSC at 190 °C. Based on the width of this diffraction, it can be judged that the low-angle diffraction is attributed to two separate diffraction peaks superimposed at $2\theta = 4.30$ and 5.00° (d-spacing of 2.06 and 1.77 nm) (Section 3.2). Meanwhile, the diffraction peak at $2\theta = 13.4°$ (d-spacing of 0.676 nm) becomes evident after the sample was cooled to below 190 °C. Based on these observations, it can be concluded that an ordered phase forms at 190 °C. Upon further cooling to room temperature, the two diffraction peaks in the low-angle region gradually merge by shifting the diffraction at $2\theta = 4.30°$ towards higher angles while the diffraction peak at $2\theta = 5.00°$ changes less during cooling. Several weak diffraction peaks also appear on top of the scattering halo. The width at half-height of the scattering halo in the wide-angle region continuously decreases during cooling.

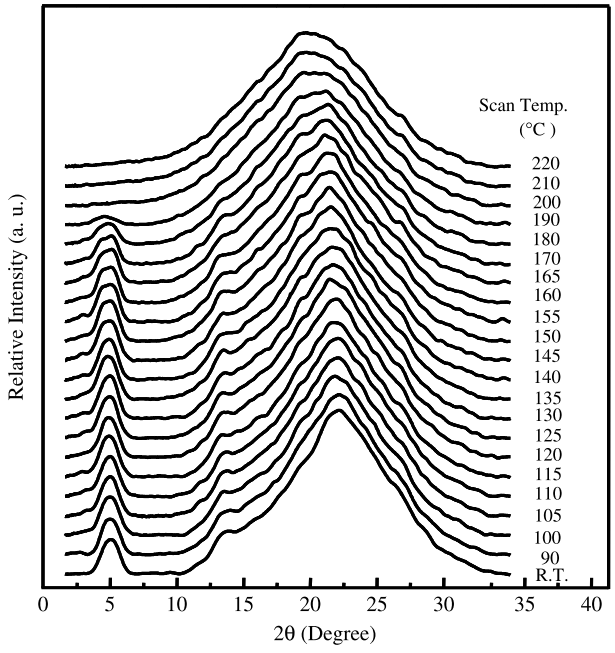

Fig. 4. Set of 1D WAXD powder patterns of BPDA–7CBBP during cooling at different temperatures (cooling rate of 2.5 °C/min).

3.2. Identifications of crystalline structures

In order to understand the structure formed by the low-temperature transition process, Fig. 5 shows a 2D WAXD fiber

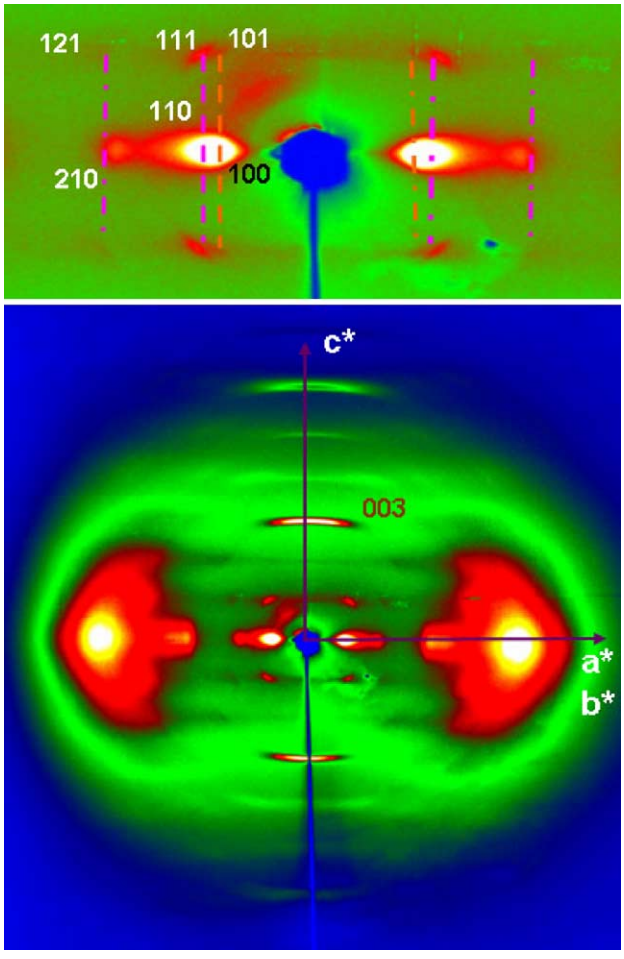

Fig. 5. A 2D WAXD fiber pattern of BPDA–11CBBP after the fibers were annealed at 210 °C and then quickly quenched to room temperature. The 2D pattern was recorded at room temperature. An enlarged 2D WAXD fiber pattern in the low 2θ-angle region is also included as an insert at the top of the figure.

Table 1
The experimental and calculated crystallographic parameters of the hexagonal phase in BPDA–11CBBP

(*hkl*)	2θ (°)$_{expt.}$	2θ (°)$_{cal.}$	*d*-Spacing (nm)$_{expt.}$	*d*-Spacing (nm)$_{cal.}$	Intensity[a]
100	4.38	4.34	2.17	2.035	vs
110	7.6	7.52	1.16	1.175	s
030	13.05	13.04	0.67	0.69	s
330	22.3	22.7	0.39	0.392	vs
101	6.23	6.13	1.42	1.44	s
121	9.4	9.71	0.94	0.91	w
022	12.6	12.28	0.70	0.72	vw
003	13.1	13.01	0.67	0.68	s
014	18.1	17.93	0.49	0.49	w
114	18.8	18.97	0.47	0.467	w
124	21.0	20.89	0.42	0.42	vw

The theoretical calculation is based on the hexagonal unit cell with $a=b=2.35$ nm, $c=2.04$, and $\alpha=\beta=90°$, $\gamma=120°$. With putting six monomers in one unit cell, the calculated density of the perfect crystal is 1.22 g/cm^3.

[a] The intensity are semi-quantitatively estimated via a microdensitometer and classified as very strong (vs), strong (s), medium (m), weak (w) and very weak (vw).

pattern of BPDA–11CBBP after the fibers were heated and annealed at 210 °C and then quickly quenched to room temperature. On the meridian, a pair of intense diffraction arcs at $2\theta=13.35°$ (*d*-spacing of 0.663 nm) can be seen. This is a typical feature of these BPDA-based polyimides and can be indexed as the (003) reflection along the fiber axis, indicating that the polyimide backbones possess an extended chain conformation along the fiber axis [31–34]. On the equator, the *d*-spacing value of one pair of strong sphere-shaped diffraction spots appears, as seen in the inset of Fig. 5 (on the top of the figure). Careful analysis indicates that this pair of spots is attributed to two overlapped diffractions at $2\theta=4.43$ and 3.95° (*d*-spacing of 1.99 and 2.24 nm), which has already been observed in 1D WAXD patterns. They are assigned to be the (110) and (100) diffractions. The assignment of the (100) diffraction can also be verified by the diffraction on the (*hk1*) layer in the quadrants, such as the (101) diffraction, and further refined by the equatorial (400) diffraction. The shapes of the diffraction arcs on the equator and quadrants are also distinct from this spherical shaped diffraction, supporting the conclusion that this strongest equatorial diffraction pair results from the merger of two diffraction arcs. A pair of diffuse scattering halos is also observed on the equator in the wide-angle region of $2\theta=21.0°$ (*d*-spacing of 0.423 nm), which is due to the lateral chain packing among the backbones and side chains. Detailed crystallographic analysis reveals that this phase possesses a large hexagonal unit cell containing six chains (K_H). By applying the least square fitting method in the refinement process [23], the dimensions of the unit cell have been determined to be $a=2.35$ nm, $c=2.04$ nm, $\alpha=90°$, $\beta=90°$, and $\gamma=120°$. The calculated crystallographic density of the K_H phase is 1.22 g/cm^3, and the experimentally measured density is 1.20 g/cm^3. The calculated and experimentally observed 2θ and *d*-spacing of the diffractions are listed in Table 1. Note that in a hexagonal lattice, chains possess a cylindrical symmetry. Therefore, the dimension of $a=2.35$ nm represents the inter-distance between two neighboring cylinders.

Fig. 6 shows a 2D WAXD fiber pattern of BPDA–9CBBP after it was annealed at 200 °C and quenched to room temperature. The complex set of diffraction pairs indicate that this crystal structure does not have high symmetry and therefore, little extinction takes place. If we enlarge the center part of Fig. 6, the diffraction pairs are not exactly located on the equator as shown in the insert of Fig. 6, rather, they are split into the quadrants (the insert on the right of Fig. 6). Therefore, this is a clear signal of a triclinic crystal lattice. Detailed crystallographic analysis shows that the crystal lattice is triclinic (K_T) with dimensions of $a=3.74$ nm, $b=1.58$ nm, $c=1.98$ nm, $\alpha=89.3°$, $\beta=91.8°$, $\gamma=70.9°$. The calculated density based on this unit cell was 1.38 g/cm^3, as compared with the experimental value of 1.36 g/cm^3. In each unit cell, there are eight repeating units in this K_T phase. The calculated and experimentally observed 2θ and *d*-spacing of these diffractions are listed in Table 2.

For the BPDA–7CBBP oriented samples, Fig. 7 shows a 2D WAXD fiber pattern after the sample was annealed at 190 °C and quenched to room temperature. The diffraction spot closest to the center along the equator is split into two diffractions (as shown in the inserts on the left bottom and right side of Fig. 7) indicating that at least one of the *a**- or *b**-axis is tilted from the equator. On each layer, pairs of diffraction spots are not located at the same level. On the other hand, the strongest diffraction pair on the meridian is again attributed to one third of the length of the chemical repeating unit in the polyimide

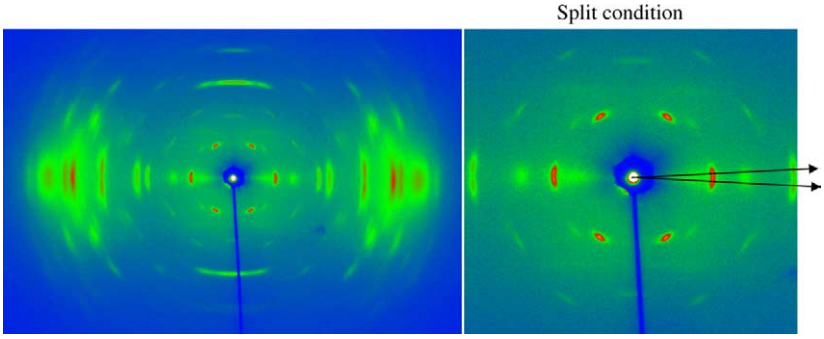

Fig. 6. A 2D WAXD fiber pattern of BPDA–9CBBP after the fibers were annealed at 200 °C and then quickly quenched to room temperature. The 2D pattern was recorded at room temperature. An enlarged 2D WAXD fiber pattern in the low 2θ-angle region is also included as an insert at the right of the figure.

Table 2
The experimental and calculated crystallographic parameters of the triclinic phase in BPDA–9CBBP

hkl	2θ (°)$_{expt.}$	2θ (°)$_{cal.}$	*d*-Spacing (nm)$_{expt.}$	*d*-Spacing (nm)$_{cal.}$	Intensity[a]
010	5.9	5.90	1.49	1.49	vs
020	11.9	11.82	0.744	0.748	s
030	17.9	17.7	0.495	0.5	s
$\bar{3}30$	21.5	21.49	0.413	0.413	vs
440	22.5	22.5	0.395	0.395	s
$\bar{6}30$	26.6	26.95	0.336	0.331	m
101	5.2	5.19	1.70	1.70	vs
$\bar{2}11$	9.9	9.87	0.893	0.896	w
$\bar{2}21$	15.4	14.88	0.575	0.595	m
012	10.4	10.68	0.850	0.828	m
032	19.6	19.82	0.452	0.448	m
$0\bar{3}2$	20.2	20.08	0.441	0.442	s
$\bar{1}32$	20.7	20.67	0.431	0.429	w
$\bar{3}32$	23.3	23.148	0.383	0.384	m
003	13.4	13.5	0.663	0.656	s
$\bar{2}13$	16.0	15.9	0.556	0.539	w
$\bar{3}23$	20.2	20.7	0.431	0.429	m

The calculated data listed are based on the triclinic unit cell with $a=3.74$ nm, $b=1.58$ nm, $c=1.98$ nm, $\alpha=89.3°$, $\beta=91.8°$, $\gamma=70.9°$.

[a] The intensity are semi-quantitatively estimated via a microdensitometer and classified as very strong (vs), strong (s), medium (m), weak (w) and very weak (vw).

backbones. Furthermore, in this crystalline form, the *c**-axis and the chain axis are tilted away from the fiber direction. Combining these observations, a conclusion can be made that we are dealing with a triclinic structure. If the *a**-axis in the crystal lattice is tilted from the equator, only the (0*k*0) diffractions are on the equator, and the (*h*00) and the (*hk*0) diffractions are located in the quadrants. By applying the refinement process, the crystal lattice was determined to possess a triclinic unit cell with dimensions of $a=2.57$ nm, $b=2.08$ nm, $c=2.02$ nm, $\alpha=84.8°$, $\beta=86.1°$, and $\gamma=83.4°$. The calculated density based on this unit cell was 1.38 g/cm^3, as compared with the experimental result of 1.36 g/cm^3, indicating that in each unit cell there are eight repeating units. The calculated and experimentally observed 2θ and *d*-spacing of these diffractions are listed in Table 3.

3.3. Liquid crystalline phase structures and building blocks

Fig. 8 shows a 2D WAXD fiber pattern of BPDA–11CBBP after the fiber sample was heated to 265 °C, which is above the melting endotherm of the K_H phase, and then quenched to room temperature. It is evident that the molecular orientation in the oriented sample along the fiber direction is maintained. Two pairs of scattering halos on the equator are observed: one pair is located at $2\theta=3.84$–$4.91°$ (*d*-spacing of 2.3–1.8 nm), and the other is at $2\theta=21.2°$ (*d*-spacing of 0.42 nm). The pair of diffractions in the low-angle region are attributed to the short-range order of the self-organized cylindrical individual chains along the direction perpendicular to the chain orientation on the nanometer scale [35]. Another scattering halo pair is due to the lateral chain packing on the sub-nanometer scale, indicating that the side chains and backbones are oriented parallel to the fiber direction (further proved by our IR results, see below). Therefore, a structure with two length scales can be observed. On the meridian, a pair of diffraction arcs at $2\theta=13.4°$ (*d*-spacing of 0.676 nm) remain. Again, it is 1/3 the length of the polyimide backbone, similar to other BPDA-based polyimide structures. No diffraction can be observed in the quadrants, revealing that the 3D ordered structure has been lost. A supra-molecular N phase structure can thus be identified in which the base unit is a combination of the backbone polyimides and LC side chains.

This N phase of BPDA–11CBBP formed at 260 °C during cooling from the I state can also be further confirmed by PLM morphological observations as shown in Fig. 9(a) and (b). For a film sample at 260 °C, *schlieren* LC textures can be observed and the sample behaves like a birefringent fluid, as shown in Fig. 9(a). When the sample is mechanically sheared at this temperature, a periodic and alternating banded texture is generated, in which the normal direction of the alternating

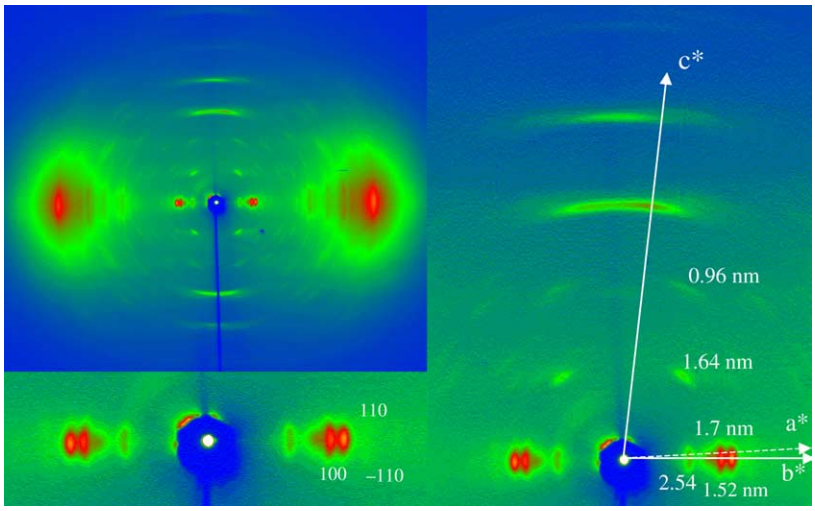

Fig. 7. A 2D WAXD fiber pattern of BPDA–7CBBP after the fibers were annealed at 190 °C and then quickly quenched to room temperature. The 2D pattern was recorded at room temperature. Two enlarged 2D WAXD fiber patterns are also included at the bottom of the left side and right side of the figure.

Table 3
The experimental and calculated crystallographic parameters of the triclinic phase in BPDA–7CBBP

hkl	2θ (°)$_{expt.}$	2θ (°)$_{cal.}$	*d*-Spacing (nm)$_{expt.}$	*d*-Spacing (nm)$_{cal.}$	Intensity[a]
100	3.48	3.47	2.54	2.54	s
110	5.21	5.21	1.69	1.69	vs
$\bar{1}10$	5.81	5.80	1.52	1.52	vs
200	6.75	6.94	1.31	1.27	w
$\bar{3}10$	11.71	11.70	0.75	0.75	w
320	12.5	12.76	0.70	0.69	w
230	13.4	13.96	0.66	0.63	s
330	16.0	15.68	0.55	0.56	m
430	18.2	17.93	0.49	0.49	m
340	19.2	19.15	0.46	0.46	s
101	5.41	5.44	1.63	1.62	m
$\bar{1}11$	7.1	7.2	1.24	1.23	m
201	8.0	8.0	1.10	1.10	w
$\bar{1}21$	10.0	10.36	0.88	0.85	w
221	10.9	10.88	0.81	0.81	vw
$\bar{2}21$	12.0	12.33	0.74	0.72	vw
231	13.85	14.19	0.64	0.62	vw
102	9.58	9.28	0.92	0.95	m
$\bar{3}02$	14.01	14.06	0.63	0.63	w
003	13.2	13.24	0.67	0.67	s
123	15.01	15.19	0.59	0.58	w
$\bar{3}03$	17.01	17.36	0.52	0.51	w
403	18.4	18.68	0.48	0.47	w

The calculated data listed are based on the triclinic unit cell with $a=2.57$ nm, $b=2.08$ nm, $c=2.02$ nm, $\alpha=84.8°$, $\beta=86.1°$, $\gamma=83.4°$.

[a] The intensity are semi-quantitatively estimated via a microdensitometer and classified as very strong (vs), strong (s), medium (m), weak (w) and very weak (vw).

bands are parallel to the shear direction, and the band spacing is 2–3 μm, as shown in Fig. 9(b). The structural formation of these bands is related to a relaxation of oriented viscoelastic LC polymer fluids after the cessation of an external shear field [36,37]. Furthermore, conventional side-chain LC polymers usually do not exhibit banded textures after mechanical shearing. This experimental observation indicates that this N phase is attributed to the combined contribution of the 4-cyanobiphenyl mesogens in the side chains and the aromatic

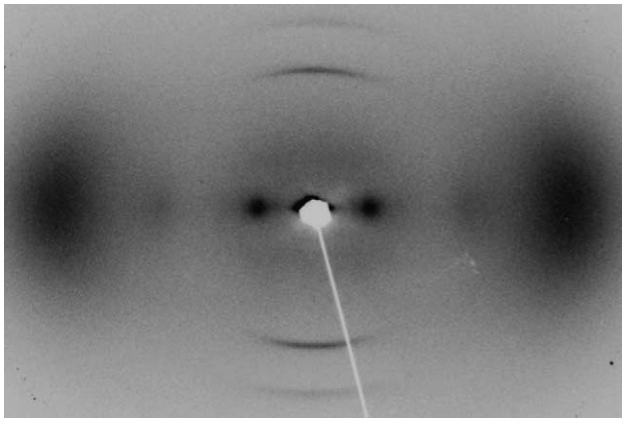

Fig. 8. A 2D WAXD fiber pattern of BPDA–11CBBP after the fibers were heated to 265 °C and then quickly quenched to room temperature. The 2D pattern was recorded at room temperature.

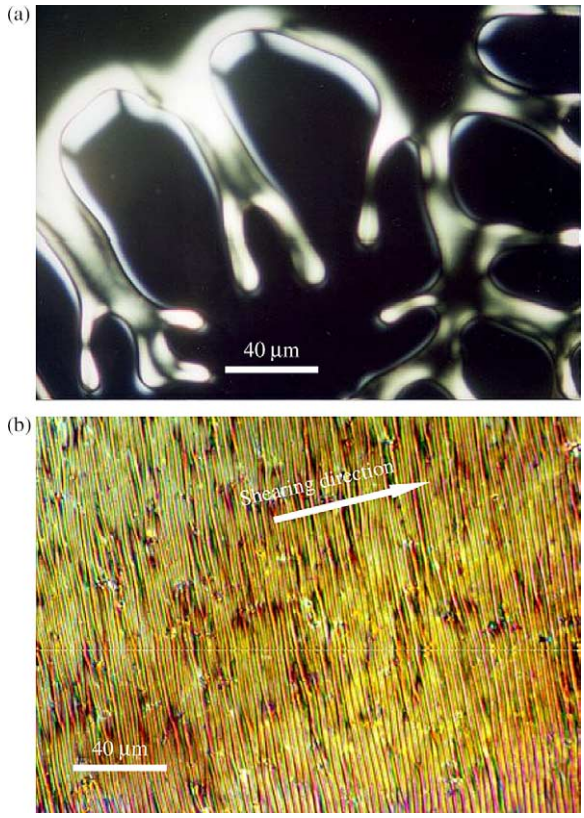

Fig. 9. PLM LC texture micrographs of BPDA–11CBBP in the high-temperature N phase of a (a) unsheared texture at 260 °C and a (b) uniaxially sheared banded texture at 260 °C.

polyimide backbones. Similar LC textures are also observed for BPDA–9CBBP and BPDA–7CBBP.

In order to visualize the base unit of these supra-molecular structures in BPDA–11CBBP, we carried out specially designed TEM experiments. We used a solution-cast thin film sample with a thickness of less than 20 nm. The film sample was then annealed at 260 °C in the LC state for several hours, and then, quenched to room temperature. Fig. 10 shows the observed morphology. Careful examination reveals that they consist of parallel aggregates of cylindrical base units. In this figure, some individual base units (single rod) can also be observed. They exhibit diameters ranging from 3 to 5 nm. Note that individual cylindrical chains possess a diameter of 2.35 nm. Therefore, those should be one or two assembled basic units to form precursors of the supra-molecular structures. The sheet-like structures can also be observed and they are attributed to a 2D assembly of these basic units, and they could have developed along the third direction to form a 3D hexagonal lattice if the sample was thicker (as shown in the insert on the left of Fig. 10). The sheet-like morphology can also be found in both of the BPDA–*n*CBBP ($n=7$ and 9) cases.

3.4. Backbone and side chain orientations in the ordered structures

In order to understand orientation of the polyimide backbones and side chains in the supra-molecular LC and

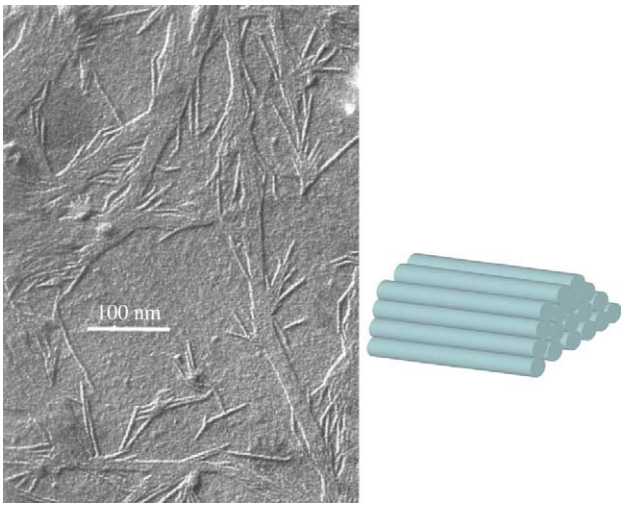

Fig. 10. TEM images of the thin films of BPDA–11CBBP after annealing at 260 °C for several hours and then, quenched to room temperature. The schematic drawing at the right side of the figure represents a stack of the cylindrical building blocks.

crystalline structures, the mechanically sheared (oriented) BPDA–*n*CBBP sample was used to measure the angular dependence of polarized FT-IR. For example, Fig. 11 shows the polarized FT-IR results of BPDA–7CBBP. By rotating the polarizing angle from 0° (parallel) to 90° (perpendicular to the shear direction), the carbonyl stretching at 1772 cm^{-1} in the imide rings exhibits an intensity decrease, so does the axial C–N stretching at 1363 cm^{-1} [38,39]. The dichroic ratios ($A_{\|}/A_{\perp}$) of the carbonyl and C–N stretching are 2.0 and 2.4, respectively. These values reveal that the polyimide backbones are oriented parallel to the orientation direction (the fiber axis in WAXD results). The cyano (CN) stretching at 2223 cm^{-1}, acting as a detectable probe of the side-chain orientation, also shows a decrease in intensity when the polarized beam change from the parallel to perpendicular with respect to the shear direction. The dichroic ratio ($A_{\|}/A_{\perp}$) of the cyano group

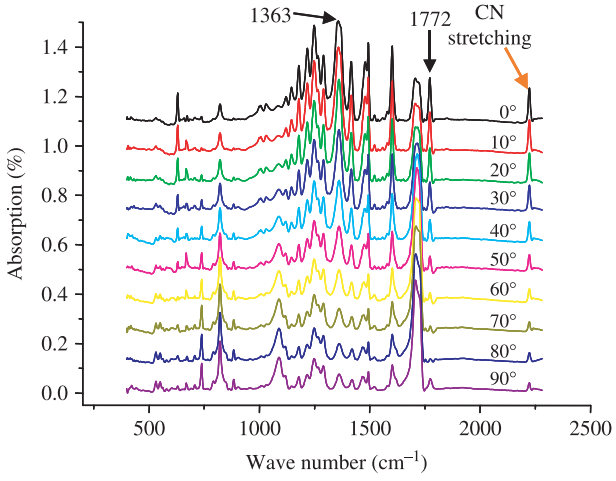

Fig. 11. Polarized FT-IR results of the uniaxially sheared BPDA–9CBBP sample recorded at room temperature. The spectra shown are by setting the polarization direction is between 0 and 90° with respect to the sample orientation direction.

stretching is 1.8, indicating that the CN group in the pendent side chains is also parallel to the orientation direction. On the other hand, the carbonyl stretching at 1716 cm^{-1} in the side chains exhibits an increase in intensity when the polarized beam changes from parallel to perpendicular to the shear direction. The dichroic ratio ($A_{\|}/A_{\perp}$) of this side-chain carbonyl stretching is 0.5, indicating that the carbonyl stretching in the side chains is perpendicular to the orientation direction. The phenylene CH out-of-plane bending at 821 cm^{-1} increases its intensity when the polarized beam is perpendicular to the shear direction, and its dichroic ratio ($A_{\|}/A_{\perp}$) is 0.45. The methylene stretching in the region of 2852 and 2925 cm^{-1} also exhibits an increase in their intensities when the polarized beam is perpendicular to the shear direction. Using the peak deconvolution procedure (purchased from Bruker software), dichroic ratios ($A_{\|}/A_{\perp}$) of asymmetric and symmetric stretching of CH_2 at 2852 and 2925 cm^{-1} were found to be 0.53 and 0.62, respectively. These bands, which arise from the aliphatic side chains, indicate that majority of CH_2 groups are also packed into the oriented direction. Combining these polarized FT-IR observations, we can conclude that both the backbones and side chains in BPDA–11CBBP are oriented parallel to the orientation direction, and therefore, one can expect that the side chains wind around outside of each polyimide backbone to form a cylindrical chain. Very similar polarized FT-IR results on BPDA–*n*CBBP ($n=7$ and 11) have also been observed.

3.5. Side-chain length dependence on the supra-molecular structural lattices

The question remains, why does the supra-molecular structure of BPDA–*n*CBBP change from the triclinic lattice when $n=7$ and 9 to the hexagonal lattice when $n=11$. Note that these two packing schemes are incomparable in symmetry. In the past, the ordered structures of most rigid backbone with flexible side chain polymers were determined to be in the arrangement that the side chains are aligned perpendicular to the aromatic backbones. For the polymers with aromatic backbones having methylene side chains terminated by 4-cyanobiphenyl mesogens, their ordered supra-molecular structure packings so far are all triclinic, and the mesogens of the side chains are packed parallel to the backbones [16–20]. No hexagonal structure has been reported.

Since, all of these structures reported are ‘supra-molecular’ in nature, namely, each molecule with both backbone and side chains constructs a basic unit, the symmetry of these units critically determine the lattice symmetry of the supra-molecular structures. This has been commonly observed in polymer lamellar single crystals. Polymer chain conformations with less rotational symmetries along the chain direction usually pack into crystal lattices with lower symmetries. For example, chain conformations with a 1_1 rotational symmetry usually lead to triclinic or monoclinic lattice. A 2_1 rotational symmetry in chain conformations usually leads to monoclinic or orthorhombic lattice. Those with a 3_1 rotational symmetry pack into a trigonal lattice; while those with a 4_1 rotational

symmetry usually are in a tetragonal lattice. The chain conformations with a 6_1 rotational symmetry generate hexagonal lattices. The geometry of conformations with a 1_1 or 2_1 rotational symmetry are asymmetric ribbon-like, while those with a 6_1 rotational symmetry are cylinder-like [40–42].

In this series of BPDA–*n*CBBP polyimides, when the number of methylene units in the side chains are relatively small ($n \leq 9$), the individual chain cannot form a cylindrical shape. Instead, they are more or less in an asymmetric ribbon-like shape. Therefore, the supra-molecular structures constructed can only be in a low symmetry lattice such as in a triclinic lattice. Note that the triclinic lattice can be explained as a layer (or even a waved-layer) packing scheme. In a parallel series of polyesters reported previously, the ordered supra-molecular lattice are triclinic, even for the polymer with eleven methylene units [16–18]. The number of methylene units may be the determining factor to control the symmetry of the overall shape of the building block. With increasing the number of methylene units, the overall shape of the individual chain (the base unit) may change from asymmetric ribbon-like to symmetric cylindrical-like, and thus, assembled supra-molecular structures reflect this change by packing the base units into a triclinic lattice or a hexagonal lattice. We have also noticed a series of LC polyesters bearing one *n*-alkoxy pendant group in each repeating unit with the number of methylene units in between four and ten (not including nine) also exhibits triclinic supra-molecular structures with a large number of waved-layer shaped basic units in each cell [43].

4. Conclusion

In summary, we have investigated a series of BPDA–*n*CBBP ($n=7$, 9, and 11) polyimides containing aromatic backbones and LC side chains. Based on the DSC and 1D WAXD experimental results, the basic phase behaviors of these polymers include two ordered phases before they enter the I state. Utilizing 2D WAXD experiments, the low-temperature phases have been characterized to be supra-molecular crystalline lattice, and the high-temperature phase is the low ordered LC N phase. It is particularly surprising to find that with an increasing number of methylene units in the side chains, the supra-molecular crystalline lattice changes from a triclinic to a hexagonal lattice. This may reflect the fact that the supra-molecular crystal lattices are critically associated with shapes of the individual chains. When the chains change from a ribbon-like to a cylindrical-like shape the supra-molecular crystal lattice correspondingly changes (from a triclinic to a hexagonal lattice).

Acknowledgements

This work was supported by the National Science Foundation, DMR-0203994 and 0516602. We also acknowledge Perkin–Elmer Co. for their support in providing a Diamond DSC instrument for our laboratory.

References

[1] Cheng SZD. J Polym Sci, Polym Phys 2005;43:3361.
[2] Frechet JM. Science 1994;263:1710.
[3] Stupp SI, Lebonheur V, Walker K, Li LS, Huggins KE, Keser M, et al. Science 1997;276:384.
[4] Muthukumar M, Ober CK, Thomas EL. Science 1997;277:1225.
[5] Zimmerman SC, Zeng F, Reichert DEC, Kolotuchin SV. Science 1996; 271:1095.
[6] Hudson SD, Jung HT, Percec V, Cho WD, Johansson G, Ungar G, et al. Science 1997;278:449.
[7] Percec V, Ahn CH, Ungar G, Yeardley DJP, Moller M, Sheiko SS. Nature 1998;391:161.
[8] Jin S, Ma YG, Zimmerman SC, Cheng SZD. Chem Mater 2004;16: 2975.
[9] Pardey R, Zhang A, Gabori PA, Harris FW, Cheng SZD, Adduci J, et al. Macromolecules 1992;25:5060.
[10] Pardey R, Shen D, Gabori PA, Harris FW, Cheng SZD, Adduci J, et al. Macromolecules 1993;26:3687.
[11] Pardey R, Wu SS, Chen J, Harris FW, Cheng SZD, Keller A, et al. Macromolecules 1994;27:5794.
[12] Kricheldorf HR, Linzer V. Polymer 1995;36:1893.
[13] Kricheldorf HR, Probest N, Wutz C. Macromolecules 1995;28: 7990.
[14] Lee M, Cho BK, Kim H, Yoon JY, Zin WC. J Am Chem Soc 1998;120: 9168.
[15] Lee M, Lee DW, Cho BK. J Am Chem Soc 1998;120:13258.
[16] Ge JJ, Zhang A, McCreight KW, Ho RM, Wang SY, Jin X, et al. Macromolecules 1997;30:6498.
[17] Ge JJ, Zhang A, McCreight KW, Wang SY, Harris FW, Cheng SZD. Macromolecules 1998;31:4093.
[18] Ge JJ, Honigfort PS, Ho RM, Wang SY, Harris FW, Cheng SZD. Macromol Chem Phys 1999;200:31.
[19] Ge JJ, Guo M, Zhang JZ, Honigfort PS, Wang SY, Harris FW, et al. Macromolecules 2000;33:3983.
[20] Ruan JJ, Ge JJ, Zhang AQ, Jin S, Wang SY, Harris FW, et al. Macromolecules 2002;35:736.
[21] Ge JJ, Xue G, Li F, Wang SY, Harris FW, Cheng SZD, et al. Macromol Rapid Commun 1998;19:619.
[22] Hong SC, Oh-E M, Zhuang X, Shen YR, Ge JJ, Harris FW, et al. Phys Rev E 2001;63:51706.
[23] Ge JJ, Li CY, Mann IK, Zhou W, Wang SY, Harris FW, et al. J Am Chem Soc 2001;123:5768.
[24] Hong SC, Oh M, Zhuang X, Shen YR, Ge JJ, Harris FW, et al. Phys Rev E 2001;63:051706–051711.
[25] Ge JJ, Hong SK, Tang BY, Li CY, Zhang D, Harris FW, et al. Adv Funct Mater 2003;13:718.
[26] Wang SY. Ph D. Dissertation, Department of Polymer Science, The University of Akron, Akron, OH 44325-3909, 1995.
[27] Ungar G, Feijoo JL, Percec V, Tound R. Macromolecules 1991;24: 953.
[28] Yandrasits MA, Cheng SZD, Zhang A, Cheng J, Wunderlich B, Percec V. Macromolecules 1992;25:2112.
[29] Yoon Y, Zhang A, Ho RM, Cheng SZD, Percec V, Chu P. Macromolecules 1996;29:294.
[30] Yoon Y, Ho RM, Moon BS, Kim D, McCreight KW, Li F, et al. Macromolecules 1996;29:3421.
[31] Cheng SZD, Arnold Jr FE, Zhang A, Hus SLC, Harris FW. Macromolecules 1991;24:5858.
[32] Cheng SZD, Wu Z, Eashoo M, Hsu SLC, Harris FW. Polymer 1991;32: 1803.
[33] Eashoo M, Wu Z, Zhang A, Shen D, Tse C, Harris FW, et al. Macromol Chem Phys 1994;195:2207.
[34] McCreight KW, Ge JJ, Guo M, Jin X, Harris FW, Cheng SZD. J Polym Sci, Polym Phys 1999;37:1633.
[35] Piao XL, Kim JS, Yun YK, Jin JI, Hong SK. Macromolecules 1997;30: 2294.

[36] Viney C, Windle AH. J Mater Sci 1983;18:1143.
[37] Hoff M, Keller A, Windle AH. J Non-Newtonian Fluid Mech 1996;67: 241.
[38] Young JT, Tasi WH, Boerio FJ. Macromolecules 1992;25:887.
[39] Perez MA, Ren Y, Farris RJ, Hsu SL. Macromolecules 1994;27: 6740.
[40] Cheng SZD, Li CY. Mater Sci Forum 2002;408:25.
[41] Cheng SZD, Lotz B. Philos Trans R Soc London, A 2003;361: 517.
[42] Cheng SZD, Lotz B. Polymer 2005;46:8662.
[43] Acierno D, Concilio S, DiMaio L, Iannelli P, Lotz B, Scarfato P. Macromolecules 2002;35:2288.